Improved Orographic Gravity Wave Drag Parameterization Accounting for the Nonhydrostatic Effect in the Weather Research and Forecasting Model: Tests for Short-Range Forecast of Northeast China Cold Vortices

Mingshan Li,[a,b] Xin Xu🅞,[a,c] Miguel A. C. Teixeira,[d] Ming Xue,[e] Haile Xue,[f] Kefeng Zhu,[g]
and Hong Huang[h]

[a] *Key Laboratory of Mesoscale Severe Weather, Ministry of Education, and School of Atmospheric Sciences, Nanjing University, Nanjing, China*
[b] *Jingmen Meteorological Service, Jingmen, Hubei, China*
[c] *CMA Radar Meteorology Key Laboratory, Nanjing, Jiangsu, China*
[d] *CEFT/FEUP, Universidade do Porto, Rua Dr Roberto Frias, Porto, Portugal*
[e] *Center for Analysis and Prediction of Storms, University of Oklahoma, Norman, Oklahoma*
[f] *CMA Earth System Modeling and Prediction Centre, Beijing, China*
[g] *Key Laboratory of Transportation Meteorology of China Meteorological Administration, Nanjing Joint Institute for Atmospheric Sciences, Nanjing, China*
[h] *College of Meteorology and Oceanography, National University of Defense Technology, Changsha, China*

ABSTRACT: The parameterization of orographic gravity wave drag (OGWD) is essential for accurate numerical weather prediction in regions of complex terrain. Current OGWD schemes assume hydrostatic orographic gravity waves (OGWs) but the parameterized OGWs in fine-resolution models with narrow subgrid-scale orography can be significantly affected by the nonhydrostatic effects (NHE). In our recent work, the OGWD scheme in the Model for Prediction Across Scales (MPAS) was revised by accounting for the NHE on the surface wave momentum flux of upward-propagating OGWs. Herein, the revised OGWD scheme is implemented in the Weather Research and Forecasting (WRF) Model to evaluate its performance in short-range weather forecast. Two sets of 36-h WRF simulations are conducted for nine Northeast China cold vortices (NECVs) that occurred in the warm season of 2011 using the original and revised OGWD schemes. Results show that the WRF Model tends to underestimate the intensity of the NECVs, producing too high geopotential height. When accounting for the NHE in the OGWD scheme, the NECV intensity biases are significantly reduced. Analyses reveal that the NHE act to weaken the lower-tropospheric OGWD by decreasing the surface wave momentum flux, which strengthens the NECV in the lower troposphere. Consequently, the strengthened low-level cyclonic circulation increases the posttrough cold advection to the southwest of the NECV which in turn enhances the NECV in the mid–upper troposphere with reduced geopotential height. The NHE are found to increase as the model horizontal resolution increases, suggesting greater importance of NHE in the OGWD parameterization of high-resolution numerical models.

KEYWORDS: Cutoff lows; Gravity waves; Subgrid-scale processes; Topographic effects; Model evaluation/performance; Parameterization

---

1. Introduction

Flow over topography can generate orographic gravity waves (OGWs), which are capable of propagating upward to the middle atmosphere (Alexander et al. 2010; Fritts and Alexander 2003; Butchart 2014). The breaking of upward-propagating OGWs can deposit wave momentum into the mean flow, resulting in a body force known as orographic gravity wave drag (OGWD), which plays an important role in driving the general circulation in the stratosphere (Sandu et al. 2019). Because of their wide spectrum, with horizontal wavelengths ranging from hundreds of meters to hundreds of kilometers, OGWs cannot be fully resolved in numerical models, with unresolved waves and their dynamical impact (i.e., OGWD) represented by subgrid-scale parameterizations.

Based on both linear and nonlinear OGW dynamics (Smith 1979; Miranda and James 1992), various OGWD parameterization schemes have been developed in the past few decades (Palmer et al. 1986; McFarlane 1987; Kim and Arakawa 1995; Lott and Miller 1997; Scinocca and McFarlane 2000; Webster et al. 2003; Kim and Doyle 2005; see also the review of Kim et al. 2003 and references therein). The implementation of OGWD parameterization schemes can help alleviate the systematic biases in both numerical weather prediction (NWP) and climate models. For example, the parameterized OGWD can decrease the westerly wind and cold pole biases in both the Northern Hemisphere and Antarctica (e.g., Palmer et al. 1986; McLandress et al. 2012; Lu et al. 2020). The simulation of regional climate and synoptic weather benefits from the parameterization of OGWD as well, examples being the East Asian summer monsoon circulation and precipitation (e.g., Choi et al. 2017; Zhang et al. 2020), the circulation and precipitation over the Tibetan Plateau (Zhou et al. 2017), and the cut-off lows in Northeast Asia (Xu et al. 2023b).

Current OGWD parameterization schemes mostly make use of the hydrostatic assumption when representing the subgrid-scale OGWs, since this significantly simplifies their formulation.

While this assumption is appropriate for coarse-resolution models with grid spacings of $O(100)$ km, in which hydrostatic waves are dominant, it is questionable in the fast-developing kilometer-scale-resolution models, such as the Integrated Forecasting System (IFS) of the European Centre for Medium-Range Weather Forecasts (ECMWF) (Polichtchouk et al. 2021) and the icosahedral nonhydrostatic model developed by the German Weather Service and the Max Planck Institute for Meteorology (Zängl et al. 2015). Although more and more OGWs are resolved as the model resolution increases, high-resolution simulations (e.g., Kruse et al. 2022) have shown that the OGWD parameterization remains important even at 3-km resolution. In fine-resolution models, the subgrid-scale orography (SSO) can be sufficiently narrow such that most of the unresolved OGWs are significantly affected by the nonhydrostatic effects (NHE). Compared with their hydrostatic counterparts, nonhydrostatic OGWs propagate not only upward but also downstream, showing a dispersive tail (Smith 1979; Klemp and Durran 1983). Due to the lateral dispersion of wave energy, the wave amplitude is reduced (Zängl 2003) which consequently affects wave breaking and OGWD. Therefore, NHE should be taken into account to more accurately represent subgrid-scale orographic effects in fine-resolution models.

In this regard, Xu et al. (2021, hereafter X21) theoretically derived the analytic formulae of surface wave momentum flux for nonhydrostatic OGWs generated by three-dimensional elliptical bell-shaped mountains. The wave momentum flux at the surface is of great importance for the parameterization of OGWD as it determines the total wave momentum that is ultimately deposited into the mean flow. The NHE depend crucially on the horizontal wind speed, the Brunt–Väisälä frequency, and the mountain width, which allows defining a nondimensional parameter called the horizontal Froude number (see X21 or section 2 below for more details). In contrast, the terrain anisotropy and horizontal wind direction have a relatively weak influence on NHE. As such, the theoretical expression of NHE for the case of isotropic orography was adopted as a good approximation by Xu et al. (2024) to correct the surface wave momentum flux in the OGWD scheme developed by Kim and Doyle (2005; hereafter KD05). (Note that the KD05 scheme has partially and semiempirically taken into account the effect of nonhydrostatic OGWD due to trapped lee waves, which was calibrated using extensive mesoscale simulations. Yet, the NHE on the vertically propagating OGWs are not considered.) Then, the revised OGWD scheme (hereafter X21 scheme) was implemented in the Model for Prediction Across Scales (MPAS) (Skamarock et al. 2012). Compared with the original KD05 scheme, the X21 scheme was found to help improve the simulation of the stratospheric polar night jet in boreal winter (Xu et al. 2024) and reduce the wintertime wet biases over the western Tibetan Plateau (Xu et al. 2023a).

While the revised OGWD scheme has been shown to be beneficial for climate simulation, its influence on the simulation of synoptic weather systems remains unclear. Herein, the X21 scheme is implemented in the Weather Research and Forecasting Model (Skamarock et al. 2019), which, like MPAS, also adopts the KD05 scheme and tests for the short-range forecast of the Northeast China cold vortex (NECV). As a type of cut-
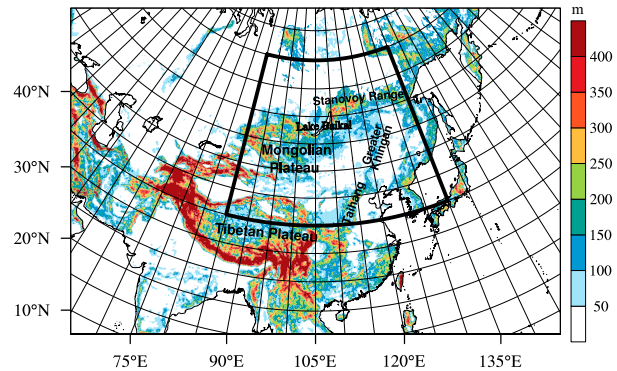

FIG. 1. Model domain and standard deviation of SSO (shading; m). The black box indicates the region of interest in Northeast Asia.

off low originating from the polar region (Nieto et al. 2005), the NECV is the most important weather system affecting Northeast China, which can cause severe convective weather like short-term intense rainfall, hail, and tornadoes (e.g., Lian et al. 2016; Luo et al. 2018; Meng et al. 2018). About half of the summer rainfall over Northeast China is attributed to the NECVs (Sun et al. 1994; Hu et al. 2010). On average, there are 7.4 NECVs per year, with each case persisting for 3–5 days (e.g., Yang and Wang 2021). NECVs most often occur in the warm season, especially in May. Our recent study (Xu et al. 2023b) showed that the complex terrain in Northeast Asia has an important influence on the NECV intensity, primarily through the OGWD caused by upward-propagating gravity waves. In this work, a series of Weather Research and Forecasting (WRF) Model simulations are conducted for nine NECV cases that occurred in the warm season (April–September) of 2011, using the original and revised KD05 schemes to evaluate the performance of the revised OGWD scheme.

The remainder of the paper is organized as follows. Section 2 describes the setup of WRF simulations, followed by a brief description of the revised OGWD parameterization scheme. Section 3 presents an overview of the nine NECV cases under examination. The influences of the revised OGWD scheme on the short-range forecast of the NECVs are studied in section 4. Finally, the paper is summarized and discussed in section 5.

2. Numerical simulations

a. Setup of numerical experiments

Figure 1 displays the WRFv4.2.1 model domain and the model's unresolved orography, i.e., SSO. The horizontal grid spacing is 9 km, along with 39 levels in the vertical. The model's top is placed at 50 hPa, accompanied by a Rayleigh damping layer in the topmost 5 km to prevent artificial gravity wave reflection at the model's top boundary. For each of the nine NECVs, two numerical experiments are conducted by using the original and revised KD05 OGWD schemes (see section 2b below). Regarding other model physics, the Yonsei University planetary boundary layer (PBL) scheme is used (Hong et al. 2006), with the new Thompson microphysics scheme (Thompson et al. 2008), the Grell–Freitas scheme for

TABLE 1. The date and location of the nine NECVs. An asterisk (*) indicates cases used for sensitivity tests.

NECV case	Initial time	End time	Notes
1*	1200 UTC 28 Apr	0000 UTC 30 Apr	Over Mongolian Plateau, decaying
2	1200 UTC 10 May	0000 UTC 12 May	Over Mongolian Plateau, developing
3*	1200 UTC 31 May	0000 UTC 2 Jun	Over Stanovoy Range, decaying
4	1200 UTC 7 Jun	0000 UTC 9 Jun	Over plain, decaying
5	1200 UTC 30 Jun	0000 UTC 2 Jul	Over plain, developing
6*	1200 UTC 5 Jul	0000 UTC 7 Jul	Over Mongolian Plateau, developing
7	1200 UTC 12 Jul	0000 UTC 14 Jul	Over plain, decaying
8	1200 UTC 1 Aug	0000 UTC 3 Aug	Over plain, developing
9	1200 UTC 12 Sep	0000 UTC 14 Sep	Over Stanovoy Range, developing

cumulus convection (Grell and Freitas 2014), the Rapid Radiative Transfer Model for general circulation models (RRTMG) longwave and shortwave radiation schemes (Iacono et al. 2008), the Fifth-generation Pennsylvania State University–National Center for Atmospheric Research Mesoscale Model (MM5) similarity scheme for the surface layer (Beljaars 1995), and the Noah land surface model (Tewari et al. 2004). The experiments using this suite of model physics are taken as the control simulations, i.e., CTL_KD05 and CTL_X21.

In addition, sensitivity experiments are performed for three particular NECV cases (i.e., Nos. 1, 3, and 6 in Table 1) using different model physics (Table 2; note that the mem01 member is just the same as the control simulation mentioned above). These cases are chosen because they are most notably affected by the revision of the OGWD scheme (see section 4). The sensitivity experiments are composited (i.e., SEN_KD05 and SEN_X21) and analyzed, in order to make the evaluation of the revised OGWD scheme more reliable (and thus the impact of the NHE more robust).

The WRF Model is integrated for 36 h (see the initial time for each case in Table 1), with the first 12 h taken as the model spinup time. The model's initial and lateral boundary conditions are derived from the 6-hourly, 0.75° ERA-Interim reanalysis data developed by the ECMWF (Dee et al. 2011; https://www.ecmwf.int/en/forecasts/dataset/ecmwf-reanalysis-interim/).

b. Revision of the KD05 OGWD scheme

In the OGWD scheme developed by KD05, the surface wave momentum flux of upward-propagating OGWs is expressed as

$$\tau_0 = \rho_0 E \frac{m}{\lambda_{\text{eff}}} G \frac{|\mathbf{V}_L|^3}{N_L}, \tag{1}$$

where

$$E = (\text{OA} + 2)^{C_E(\text{Fr}_0/\text{Fr}_c)}, \quad m = (1 + L_x)^{\text{OA}+1},$$

$$G = \frac{\text{Fr}_0^2}{\text{Fr}_0^2 + C_G \text{OC}^{-1}}, \quad \text{Fr}_0 = \frac{2\sigma_h N_L}{|\mathbf{V}_L|} \text{OD}. \tag{2}$$

The "number of mountains" within the model grid cell (i.e., m) is used to measure the bulk volume of the SSO. The factor λ_{eff} is a tunable coefficient indicating the effective grid length, which is practically set to be 3 times the grid spacing in the WRF Model. The coefficient E denotes the drag enhancement by the low-level wave breaking and/or lee wave trapping

TABLE 2. Configurations of WRF Model physics.

Name	Microphysics	PBL	Surface layer	Radiation scheme (long)	Radiation scheme (short)
mem01 (CTL)	Thompson	YSU	MM5	RRTMG	RRTMG
mem02	Thompson	YSU	MM5	Dudhia[a]	Dudhia
mem03	Thompson	MYJ[b]	Monin–Obukhov[c]	RRTMG	RRTMG
mem04	Morrison2-mom[d]	ACM2[e]	MM5	CAM[f]	CAM
mem05	Thompson	MYJ	Monin–Obukhov	Goddard[g]	Goddard
mem06	Morrison2-mom	YSU	MM5	Dudhia	Dudhia
mem07	Morrison2-mom	YSU	MM5	Goddard	Goddard
mem08	Morrison2-mom	ACM2	MM5	Dudhia	Dudhia
mem09	Morrison2-mom	YSU	MM5	RRTMG	RRTMG
mem10	Morrison2-mom	MYNN2[h]	MM5	Dudhia	Dudhia

[a] Dudhia (1989)
[b] Janjić (1994)
[c] Jiménez et al. (2012)
[d] Morrison et al. (2009)
[e] Pleim (2007)
[f] Collins et al. (2004)
[g] Matsui et al. (2018)
[h] Nakanishi and Niino (2006)

subject to the shape and location of the SSO within the grid cell as well as the flow nonlinearity measured by the nondimensional mountain height Fr_0. According to the criterion of $Fr_c = 1$, the coefficient G provides a smooth transition between flow blocking/nonblocking by the SSO. The variable σ_h denotes the standard deviation of the SSO height, and L_x is the effective SSO length along the direction of low-level mean flow $\mathbf{V}_L$ obtained by averaging the horizontal winds between the surface and $2\sigma_h$ above the surface. The nondimensional orographic asymmetry (OA) measures the subgrid-scale terrain asymmetry and its position relative to the model grid box. The orographic convexity (OC) indicates the sharpness and slope of the terrain. The nondimensional orographic direction (OD) reflects the orography anisotropy defined as $OD \equiv L_x^{\perp}/L_x$, with $L_x^{\perp}$ being the orography width in the direction normal to the low-level mean wind $\mathbf{V}_L$. The low-level mean air density (ρ_0) and buoyancy frequency (N_L) are obtained in a similar manner to $\mathbf{V}_L$. The variables $C_E = 0.8$ and $C_G = 0.5$ are two constants empirically calibrated using mesoscale numerical simulations (Kim and Arakawa 1995). Once the OGWs are launched, they propagate upward level by level until they encounter a critical level or break due to wave saturation. Readers are referred to KD05 for more details about this scheme.

While the NHE can affect many aspects of OGWs, it is herein referred to as the reduction of surface wave momentum flux of upward-propagating OGWs by the trapping of very short OGWs (which are thus vertically evanescent) and the lateral dispersion of longer OGWs (X21; Smith 1979). To account for the NHE, τ_0 in Eq. (1) is revised as

$$\tilde{\tau}_0 = \tau_0[1 + \text{NHE}_c(\text{Fr})], \tag{3}$$

with $\text{NHE}_c(\text{Fr})$ denoting the correction by the NHE given by

$$\text{NHE}_c(\text{Fr}) = -\frac{9}{8}\text{Fr}^2$$
$$+ e^{-2\text{Fr}^{-1}}\left(-\frac{5}{4}\text{Fr}^{-2} - \frac{1}{2}\text{Fr}^{-1} + \frac{5}{4} + \frac{9}{4}\text{Fr} + \frac{9}{8}\text{Fr}^2\right), \tag{4}$$

which is theoretically derived in X21. The horizontal Froude number $\text{Fr} = |\mathbf{V}_L|/(N_L L_x)$ is used to quantify the degree of nonhydrostaticity, which increases as Fr grows. For simplicity, the deduction of these equations is not replicated here but can be found in X21. Readers are also referred to Xu et al. (2024), which describes the revision of the KD05 OGWD scheme at length.

3. Overview of the NECV cases

Figure 2 shows the geopotential height (GPH) and temperature at 500 hPa for the nine NECV cases under consideration, which were obtained from the hourly, 0.25° ERA5 reanalysis (Hersbach et al. 2018; https://www.ecmwf.int/en/forecasts/dataset/ecmwf-reanalysis-v5). While all these NECV cases occurred in Northeast Asia (see the black box in Fig. 1), their locations differed considerably. NECV cases 1 and 6

were closer to the Mongolian Plateau, i.e., in the western part of the region of interest (Figs. 2a,f). On the contrary, the centers of the NECV in cases 4, 7, and 8 were located over the eastern plain of this region (Figs. 2d,g,h). In the remaining cases, the NECV was located in the middle part of this region, with its center close to Lake Baikal, except in case 2 (Figs. 2b,c,e,i). Among all these NECVs, cases 1 and 2 are the strongest (i.e., 500-hPa GPH minimum lower than 5400 gpm; Figs. 2a,b), followed by cases 3, 4, and 9 with the 500-hPa GPH minimum ranging from 5400 to 5500 gpm (Figs. 2c,d,i). The NECVs in cases 5, 6, 7, and 8 are the weakest, with their 500-hPa GPH minimum above 5500 gpm (Figs. 2e–h).

Figure 3 shows the evolution of the NECV intensity (denoted by the mean GPH averaged within a 1° × 1° box centered at the 500-hPa GPH minimum as in Xu et al. 2023b) for the nine cases. In general, the NECV cases 1, 3, 4, and 7 show a weakening trend (i.e., increasing GPH) during the 24-h forecast time (Figs. 3a,c,d,g), given the relatively high GPH at the end of forecast. (Note that the 24-h forecast is from 12 to 36 h into the simulation because the initial 12 h are taken as the model's spinup time.) For example, the initial 500-hPa GPH of NECV case 1 is 5268 gpm, but it eventually reaches 5308 gpm (Fig. 3a). In contrast, the intensities of NECV cases 2, 5, 6, 8, and 9 are enhanced (i.e., the GPH decreases) during the 24-h forecast (Figs. 3b,e,f,h,i). More precisely, their intensities first decline (with growing GPH) but then increase (with falling GPH), especially for case 9 which shows a large variation of GPH of ~70 gpm (Fig. 3i).

According to the above analyses of Figs. 2 and 3, the nine NECV cases occurred at different times (from April to September) and locations (from western to eastern Northeast Asia, with different underlying orography) and had different evolutions of intensity (either developing or decaying). Thus, the revised OGWD scheme is evaluated for a considerably diverse range of NECVs.

4. Results of WRF simulations

a. Forecast biases of the simulated NECVs

The intensities of the nine NECV cases in the control simulations are shown in Fig. 3 as well. Overall, the intensities of these NECV cases are underestimated by the WRF Model, as shown by the larger 500-hPa GPH. The only two exceptions are NECV cases 1 and 4, which are stronger than their ERA5 counterparts during the later period of forecast. In spite of these biases, the WRF Model captures the evolution of the NECV intensity fairly well, e.g., the weakening (strengthening) before (after) 21 h into the simulation for NECV case 8 is similar to that in ERA5 (Fig. 3h). By contrast, timing biases are found for some NECV cases, e.g., case 5 (Fig. 3e) exhibits a time lag of 3 h in reaching the largest 500-hPa GPH. Furthermore, the trend of NECV intensity as simulated by the WRF Model occasionally deviates from that of ERA5. For instance, the intensity of NECV case 3 continues to decrease after 25 h into the simulation, which differs from the increasing trend in ERA5 (Fig. 3c).
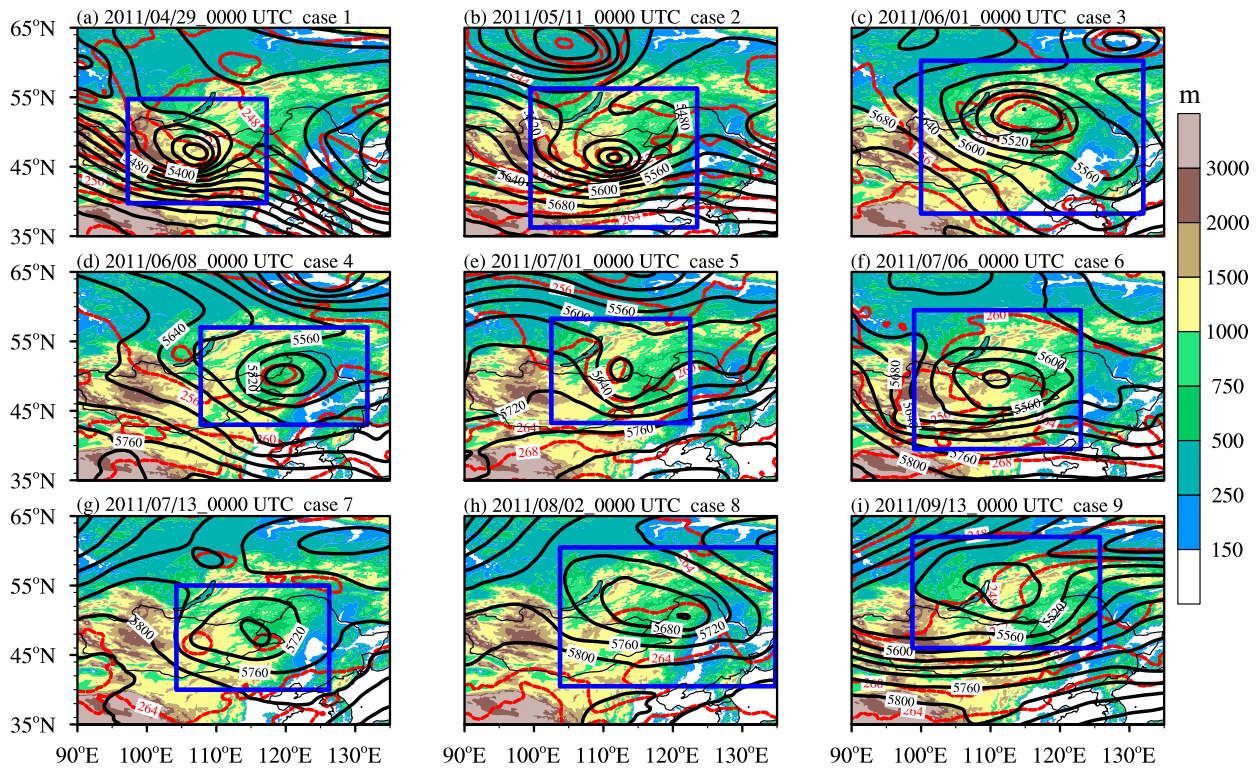
FIG. 2. GPH (black contours; gpm) and temperature (red contours; K) at 500 hPa for the nine NECV cases obtained from the ERA5 reanalysis. The color shading shows the model-resolved orography (m). The blue boxes indicate the regions, where the areal-mean horizontal wind speed, which are chosen based on the size of the NECV. The times of these NECV cases are indicated on the top left of each subplot.

The model biases in the NECV intensity are more clearly displayed in Fig. 4. For each of these nine cases, the mean biases averaged during the 24-h forecast are given in the figure upper-left corner. All the time-mean biases of 500-hPa GPH are positive. For the experiments using the original KD05 scheme, relatively large biases are found for the NECV cases 5, 8, and 9 which exceed 20 gpm (Figs. 4e,h,i). Albeit large, these biases are at least comparable to that in Fan et al. (2023; Fig. 1) which studied a NECV case using 3-km WRF simulation. Moderate biases of between 10 and 20 gpm are found for cases 2, 6, and 7 (Figs. 4b,f,g). The biases are the smallest for NECV cases 1, 3, and 4 (Figs. 4a,c,d), especially the latter, which is only 2.5 gpm.

Of greater interest is the difference between the intensities in the two sets of experiments using the original and revised OGWD schemes. As shown in Fig. 4, there is a decrease of intensity bias for all the NECV cases except case 8 when using the revised OGWD scheme. The most notable alleviation is found for NECV cases 1 and 6, with their 500-hPa GPH biases decreased by ∼3.5 gpm during the 24-h forecast (Figs. 4a,f). This is because these NECV cases are located close to the Mongolian Plateau (Figs. 2a,f) where the underlying terrain is considerably complex, resulting in greater NHE (see section 4b). The model biases are moderately alleviated for the NECV cases 2, 3, and 9 between 1.0 and 2.5 gpm (Figs. 4b,c,i). These NECVs are mainly influenced by the relatively low topography of the Stanovoy Range to the northeast and south of Lake Baikal (Figs. 2b,c,i).

For the other four NECV cases 4, 5, 7, and 8 (Figs. 4d,e,g,h), the intensity biases in CTL_X21 are either very weakly reduced (e.g., 0.1 gpm in Fig. 4g) or increased (e.g., 0.1 gpm in Fig. 4h) compared to that in CTL_KD05. This indicates trivial NHE, as these NECV cases are mainly located over a flat area.

Figure 5a depicts the evolution of the mean intensity of the nine NECV cases. The mean 500-hPa GPH obtained from the ERA5 reanalysis first increases from 5490 to 5512 gpm in 9 h and then drops to 5494 gpm again in the following 15 h. The overall evolution of the mean 500-hPa GPH is captured by the WRF Model, in spite of an underestimation of the NECV intensity and a 2-h delay in reaching the maximum GPH. For the nine-case mean, the 500-hPa GPH bias is 15.4 gpm during the 24-h forecast in CTL_KD05, which is decreased to 13.9 gpm in CTL_X21, that is, reduced by 9.7%. The decrease in the mean bias is statistically significant at the 95% confidence level, as revealed by the p value of 0.037 using the Student's t test. The GPH biases at levels other than 500-hPa were examined as well, showing similar results to that in Fig. 5a (not shown).

Regarding the three NECVs cases 1, 3, and 6 that are most notably affected by the OGWD, their 500-hPa GPH biases are reduced up to 27% (Fig. 5b) for the 24-h forecast, which is much larger than the nine-case mean (Fig. 5a). The p value is 0.011 which clearly passes the 95% significance test (i.e., a t test for the mean forecast bias of the nine cases for CTL_KD05 and CTL_X21). Besides the control simulation (i.e., mem01 in
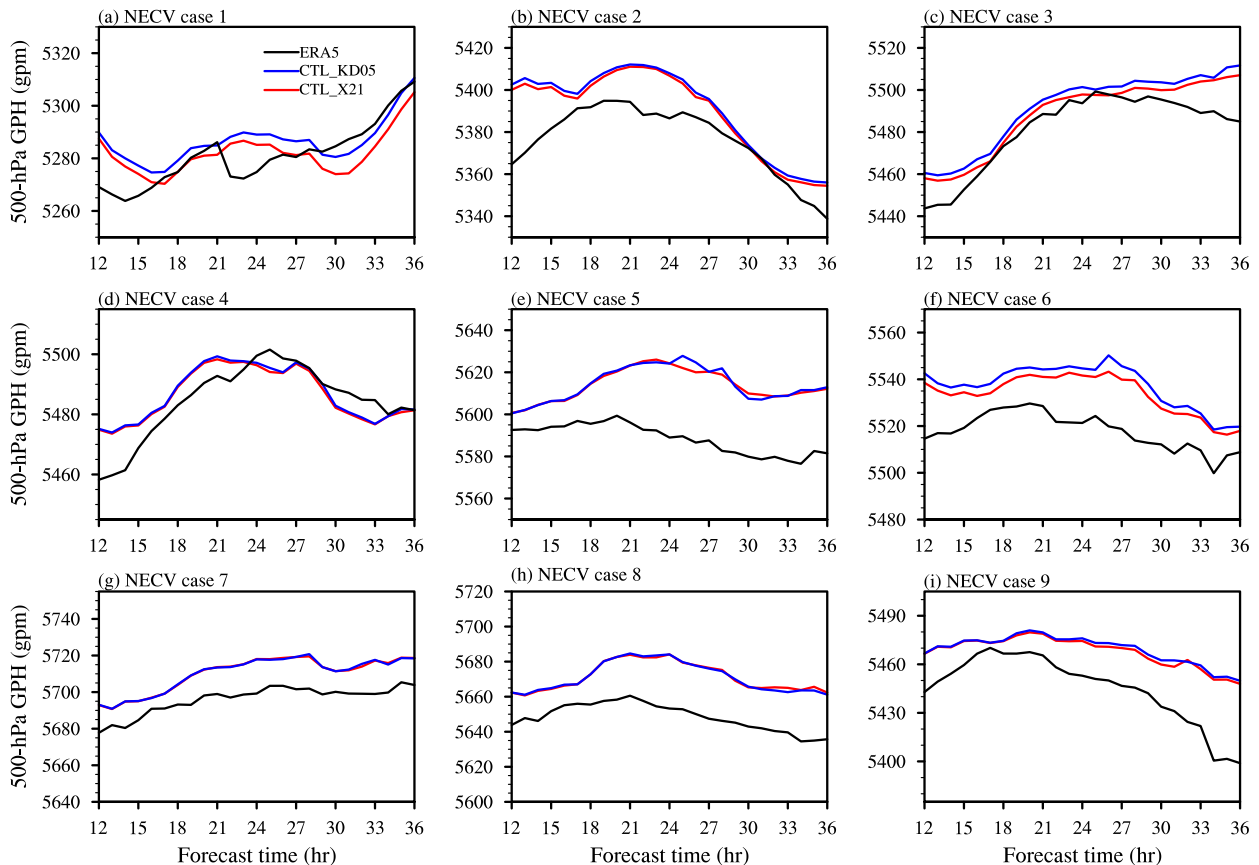
FIG. 3. Temporal evolution of mean 500-hPa GPH (gpm) averaged within a box of $1° \times 1°$ around the NECV center for the nine NECV cases obtained from the ERA5 reanalysis (black lines) and the WRF simulations of CTL_KD05 (blue lines) and CTL_X21 (red lines), respectively.

Table 2), another nine sensitivity experiments (i.e., mem02–mem10 in Table 2) have also been conducted for the three NECV cases 1, 3, and 6 using different model physics (see section 2a). As shown in Fig. 6, for each of the sensitivity experiments, the 500-hPa GPH bias averaged during the 24-h forecast is decreased when using the revised OGWD scheme. The relative bias reduction ranges from 17% (mem07) to 62% (mem10), with a composite mean of 29% (i.e., 10.7–7.6 gpm). This mean bias decrease is also statistically significant at the 95% confidence level, with a p value of 0.012.

From the above analyses, accounting for the NHE in the OGWD scheme can significantly alleviate the underestimation of the NECV intensity by the WRF Model, which is robust as confirmed by the sensitivity experiments using different configurations of model physics. Note that there are still considerable biases when using the revised OGWD scheme. This suggests that there should be more processes other than OGWD causing the biases, but addressing those processes is beyond the scope of this study. In the next section, we will explore how the NHE affect the parameterized OGWD and hence the NECV intensity.

b. NHE on the parameterized OGWD

Figure 7a depicts the geographical distribution of the OGWD integrated from surface to the model top and averaged during

the 24-h forecast in CTL_KD05. Most of the column-integrated OGWD is located to the southwest of Lake Baikal (i.e., over the Mongolian Plateau) with a maximum value of over 9×10^{-4} Pa m s^{-2}. There is also salient OGWD to the east of Lake Baikal, with a magnitude of $6 \sim 7 \times 10^{-4}$ Pa m s^{-2}. The OGWD is less than 1×10^{-4} Pa m s^{-2} to the south of Lake Baikal and even weaker ($<0.1 \times 10^{-4}$ Pa m s^{-2}) in the plain area of Northeast China. Generally, the spatial pattern of the column-integrated OGWD agrees with that of the SSO (Fig. 1). The large standard deviation of the SSO (which denotes the magnitude of the subgrid orographic forcing) over the Mongolian Plateau and Stanovoy Range is conducive to the generation and breaking of large-amplitude OGWs and hence substantial OGWD.

Figure 7b shows the difference between the column-integrated OGWD in CTL_X21 and CTL_KD05. The OGWD tends to be reduced when taking into account the NHE, as shown by the predominantly negative differences. This is as expected because the NHE act to decrease the surface wave momentum flux of OGWs in theory [see X21 and Eq. (4)]. Yet, enhancement of OGWD is also found in a few isolated regions despite with much weaker magnitude. This may be caused by the interaction between the parameterized OGWD and resolved model flow. The weakening of surface wave
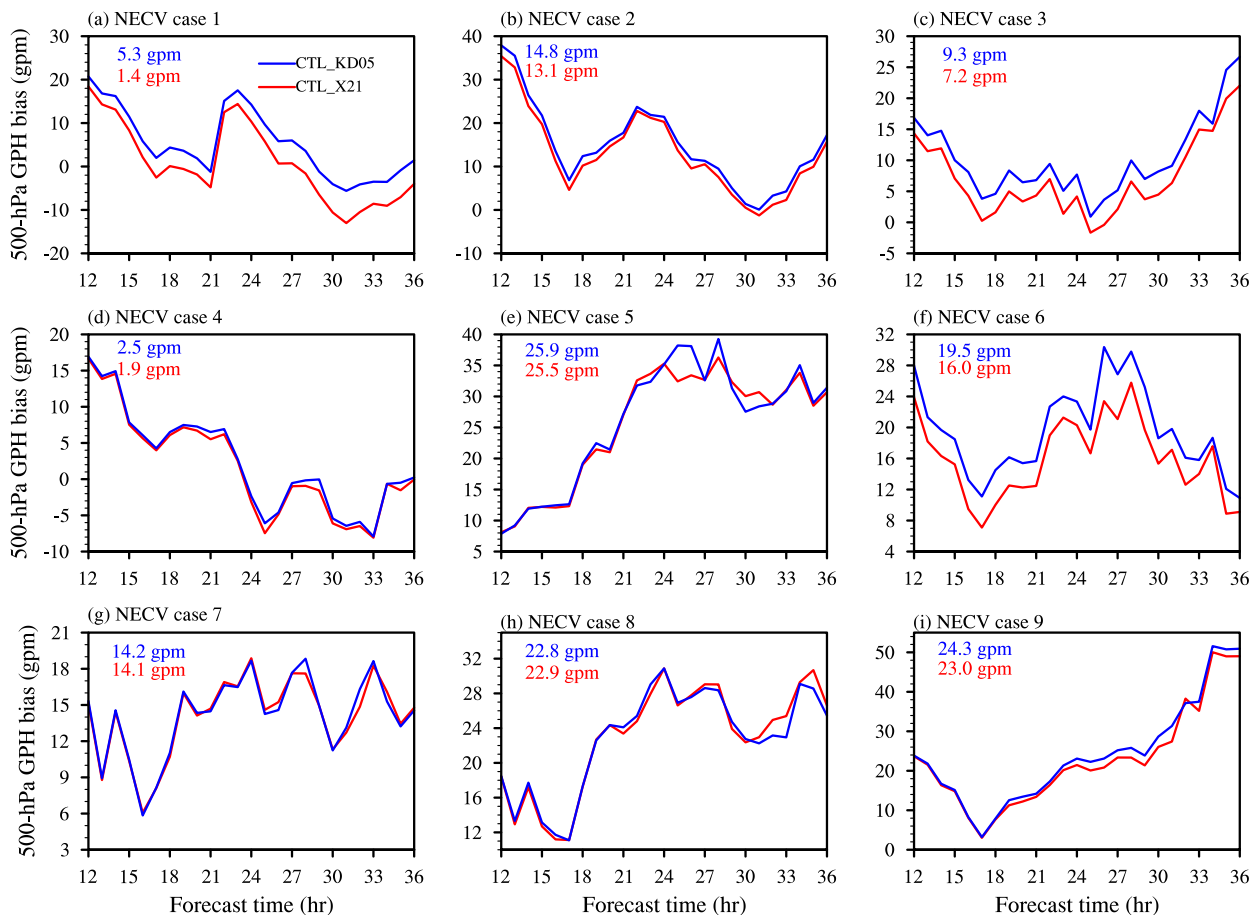
FIG. 4. As in Fig. 3, but for the model biases of GPH (gpm) with respect to ERA5. Numbers on the upper-left corner of each panel are the GPH bias averaged over the period of 12–36 h into the simulation, with blue for CTL_KD05 and red for CTL_X21.

momentum flux by the NHE may first lead to a reduction of low-level OGWD and hence an increase of low-level wind speed, which in turn enhances the surface wave momentum flux and OGWD (Xu et al. 2024).

The greatest decrease of column-integrated OGWD occurs to the southwest of Lake Baikal, exceeding -4×10^{-4} Pa m s^{-2}. The OGWD near the Taihang Mountains is also evidently reduced, suggesting important NHE there. As shown in X21, the intensity of the NHE can be quantified by the horizontal Froude number. Figure 8a is similar to Fig. 7a but displays the geographical distribution of the mean Fr averaged during the 24-h forecast in CTL_X21. (Note that the horizontal Froude number is calculated online from the simulations using the revised OGWD scheme.) Figure 8b shows the distribution of the theoretical NHE correction according to Eq. (4) which is always negative. In the regions of complex terrain, e.g., the Mongolian Plateau, Stanovoy Range, and Taihang Mountain (Fig. 1), Fr can exceed 0.3, corresponding to large NHE of over -15% in theory. The two centers of strong NHE located to the southwest of Lake Baikal and near the Taihang Mountains agree with the significant reduction of OGWD there (Fig. 7b). However, for the NHE maxima located to the due south of Lake Baikal (around 48°N), there is little decrease of

OGWD (Fig. 7b). This is due to the fact that the OGWD itself is weak in that region (Fig. 7a).

In addition to the column-integrated OGWD, Fig. 9a displays the evolution and vertical distribution of the nine-case mean OGWD averaged within the boxes encompassing the NECV (see Fig. 2) in CTL_KD05. The two NECV cases 6 and 7, shown in Figs. 9c and 9e for comparison, are located close to the Mongolian Plateau characterized by complex terrain and in the relatively flat region to the southeast of Lake Baikal, respectively. The OGWD mainly occurs in the lower troposphere below 600 hPa, with the maximum ($>1 \times 10^{-4}$ m s^{-2}) near 850 hPa at 25–30 h into the simulation (Fig. 9a). For the NECV case 6 (Fig. 9c), the OGWD extends upward to 300 hPa and shows stronger maxima of over 1.2×10^{-4} m s^{-2}. By contrast, the OGWD in NECV case 7 (Fig. 9e) is confined to the lower troposphere below 700 hPa and is much weaker.

Figures 9b, 9d, and 9f show the differences between the OGWD in CTL_X21 and CTL_KD05. For the nine-case mean (Fig. 9b), the OGWD is reduced by more than 1×10^{-5} m s^{-2} near 800 hPa around 24–27 h into the simulation. That means the OGWD is weakened by more than 10% owing to NHE. A comparable reduction is found for the OGWD at 800 hPa in NECV case 6 (Fig. 9d), while the OGWD is reduced by less
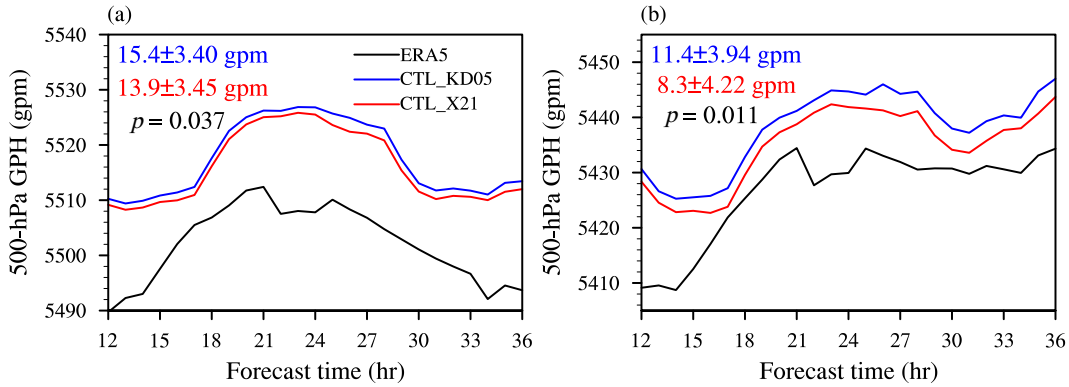
FIG. 5. Temporal evolution of 500-hPa GPH (gpm) averaged within a box of $1° \times 1°$ around the NECV center obtained from the ERA5 reanalysis (black lines) and the WRF simulations of CTL_KD05 (blue lines) and CTL_X21 (red lines). (a) Nine-NECV case mean. (b) The mean of NECV cases 1, 3, and 6. The colored numbers in the upper-left corner are the mean GPH biases and standard deviations averaged over the period of 12–36 h into the simulation, with blue for CTL_KD05 and red for CTL_X21. The black number on the upper-left corner is the p value of the Student's t test for the difference between the mean biases.

than 0.4×10^{-5} m s^{-2} in NECV case 7 (Fig. 9f). The stronger and weaker NHE in these two cases are consistent with the higher SSO over the Mongolian Plateau and the lower SSO to the southeast of Lake Baikal (Fig. 1). This explains why the intensity of some NECV cases is notably affected by the revision of the OGWD scheme while that of others is not (Fig. 4).

c. Mechanism for the influence on the NECV intensity

Given its large NHE, NECV case 6 is chosen to investigate how the changes of OGWD affect the NECV intensity. Alpert et al. (1996) revealed the importance of lower-tropospheric OGWD on cyclogenesis intensity. Xu et al. (2023b) found a two-fold impact of lower-tropospheric OGWD on the GPH of the NECV. On one hand, it can directly weaken the cyclonic circulation of the NECV in the lower troposphere and increase the GPH under the constraint of quasigeostrophic (QG) vertical vorticity. On the other hand, it can indirectly enhance the GPH

in the mid–upper troposphere, due to the suppressed cold advection to the southwest of the NECV in the lower troposphere. As shown below, this twofold impact of low-level OGWD on the NECV weakens in CTL_X21 because the OGWD is decreased by the NHE (Fig. 9d).

Figure 10a presents the spatial distribution of the QG horizontal wind, GPH, temperature, and horizontal advection of
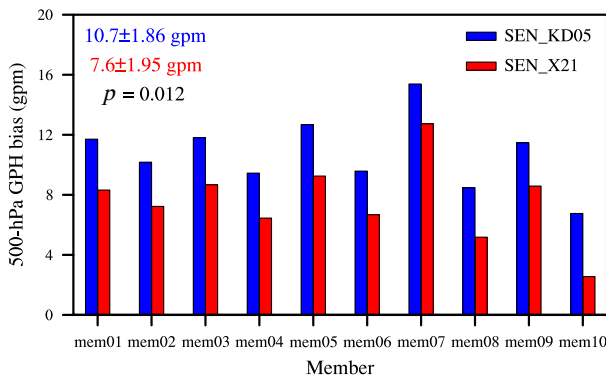

FIG. 6. The 24-h mean bias of 500-hPa GPH averaged within a box of $1° \times 1°$ around the NECV center for the sensitivity experiments of the NECV cases 1, 3, and 6. The colored numbers in the upper-left corner indicate the composite mean biases and standard deviations, with the black number denoting the p value of the Student's t test for the difference between them.
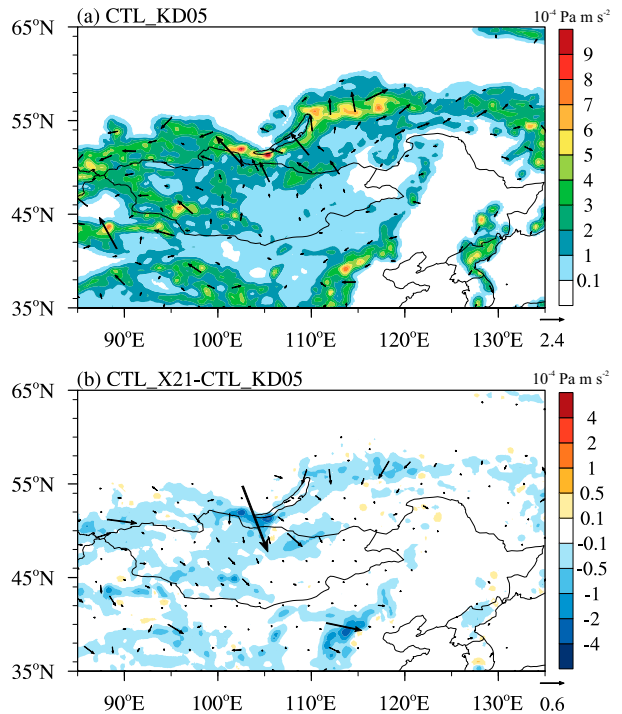

FIG. 7. Geographical distribution of the nine-case mean (a) vertically integrated OGWD field (vectors) and magnitude (shading; 10^{-4} Pa m s^{-2}) in CTL_KD05 averaged between 12 and 36 h into the simulation. (b) The difference between CTL_X21 and CTL_KD05, i.e., CTL_X21 − CTL_KD05.
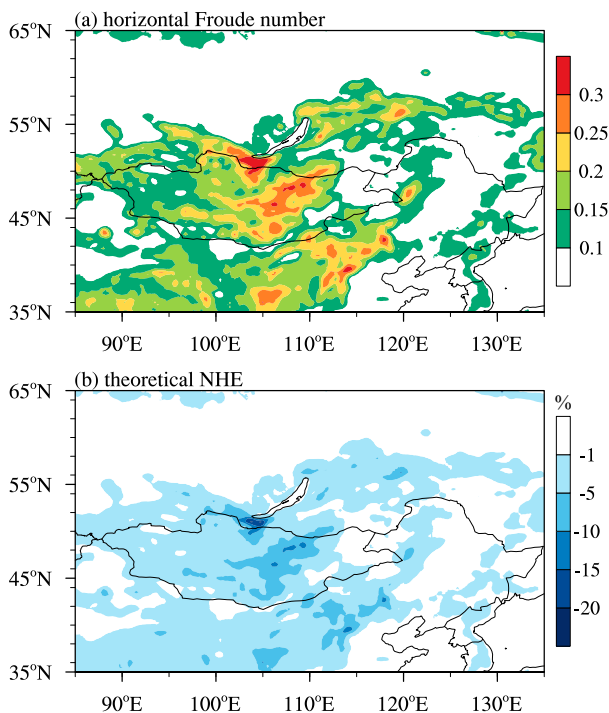
FIG. 8. Geographical distribution of the nine-case mean (a) horizontal Froude number and (b) theoretical NHE correction (%) in CTL_X21 averaged between 12 and 36 h into the simulation.

temperature at 800 hPa averaged during the period of 24–30 h into the simulation of CTL_KD05 for NECV case 6. The QG fields are obtained by applying a low-pass Barnes-type filter (Barnes 1973; Wei et al. 2023) to the model output which can effectively eliminate disturbances shorter than 1500 km (the response function of this filter is displayed in Fig. 11 of Xu et al. 2023b). This period is chosen because it is when both the lower-tropospheric OGWD and its reduction by the NHE are most remarkable (Figs. 9c,d). The NECV temperature trough lags that of GPH, such that a cold air mass is brought by the posttrough northwesterlies to the southwest of the NECV (i.e., cold advection). In CTL_X21, the OGWD is reduced by the NHE (Fig. 9d) such that the low-level winds are enhanced. This is clearly shown in Fig. 10b, as evidenced by the differential (i.e., CTL_X21 minus CTL_KD05) cyclonic circulation. In response to this enhanced cyclonic circulation, the posttrough northerlies intensify, yielding a stronger cold advection than in CTL_KD05. In fact, the posttrough cold advection is strengthened throughout the mid–lower troposphere, in particular near 750 hPa, which favors the deepening of the trough aloft and thus helps alleviate the positive GPH biases in the mid–upper troposphere.

d. Sensitivity of NHE to the model's horizontal resolution

According to the definition of horizontal Froude number, the NHE depend critically on the horizontal scales of the orography, which are thus expected to play a more important role in high-resolution models. At fine resolutions, relatively

small SSO is conductive to the generation of more nonhydrostatic OGWs. On the contrary, the primary scale of the SSO is broad at coarse resolutions which tends to produce predominantly hydrostatic waves. To explore the sensitivity of the NHE to the model's horizontal resolution, four simulations are conducted for NECV case 6 using a finer resolution of 3 km (i.e., CTL_KD05_3km and CTL_X21_3km) and a coarser resolution of 27 km (i.e., CTL_KD05_27km and CTL_X21_27km), respectively, in addition to the 9-km resolution simulation discussed in section 2a. These sensitivity experiments share the same model physics as the control simulation, except that the parameterization of cumulus convection is turned off in the 3-km-resolution simulation.

Figure 11a is similar to Fig. 3f but for the intensity of NECV case 6 simulated by using different model resolutions of 3 and 27 km. As with the 9-km resolution, the model can capture the overall evolution of the NECV intensity at both coarser and finer resolutions. In all cases, the intensity of the NECV is also underestimated, showing a higher 500-hPa GPH than ERA5. Interestingly, the underestimation is more pronounced at 3-km resolution than at 9- or 27-km resolutions. The mean GPH bias in the 24-h forecast is 26.9 gpm in CTL_KD05_3km but only 17.8 gpm in CTL_KD05_27km (Fig. 11b). The worse performance of the 3-km resolution simulation is possibly due to the fact that the WRF Model parameterization produces too much OGWD at high resolutions. Earlier studies (e.g., Sandu et al. 2019) have suggested a cutoff resolution of ~5 km for OGWD parameterization, which might mean that we are extending the OGWD parameterization to near (or beyond) its applicability limits in the 3-km resolution simulations. To test this, an additional experiment (CTL_NoOGWD_3km) is performed which is the same as CTL_KD05_3km but without an OGWD parameterization. As shown in Fig. 11, turning off the parameterization of OGWD at 3-km resolution does reduce the model bias. This suggests that the parameterization of OGWD may be unnecessary at 3-km resolution, at least for the NECV case 6, although other studies (e.g., Kruse et al. 2022) argued that the OGWD parameterization remains important even at such resolutions. Nonetheless, the issue of at what resolution an OGWD parameterization becomes unnecessary is beyond the scope of this work. Herein, we are mostly interested in the behavior of the NHE at different resolutions.

When taking into account the NHE in the OGWD scheme, the simulation of the NECV intensity is improved at all model resolutions. The mean GPH bias during the 24-h forecast decreases from 26.9 to 19.8 gpm in CTL_X21_3km while it decreases from 17.8 to 17.6 gpm in CTL_X21_27km (admittedly a very small improvement). Compared with the experiments using the original KD05 OGWD scheme, the GPH biases are reduced by 1.1%, 17.9%, and 26.4%, respectively, at 27-, 9-, and 3-km resolutions. That is, from coarser to finer resolutions, the impact of the revised OGWD scheme on the NECV intensity increases progressively.

Figures 12a–c show the geographical distributions of the horizontal Froude number at different model resolutions for NECV case 6, while Figs. 12d–f are the corresponding theoretical NHE obtained from Eq. (4). As the model resolution
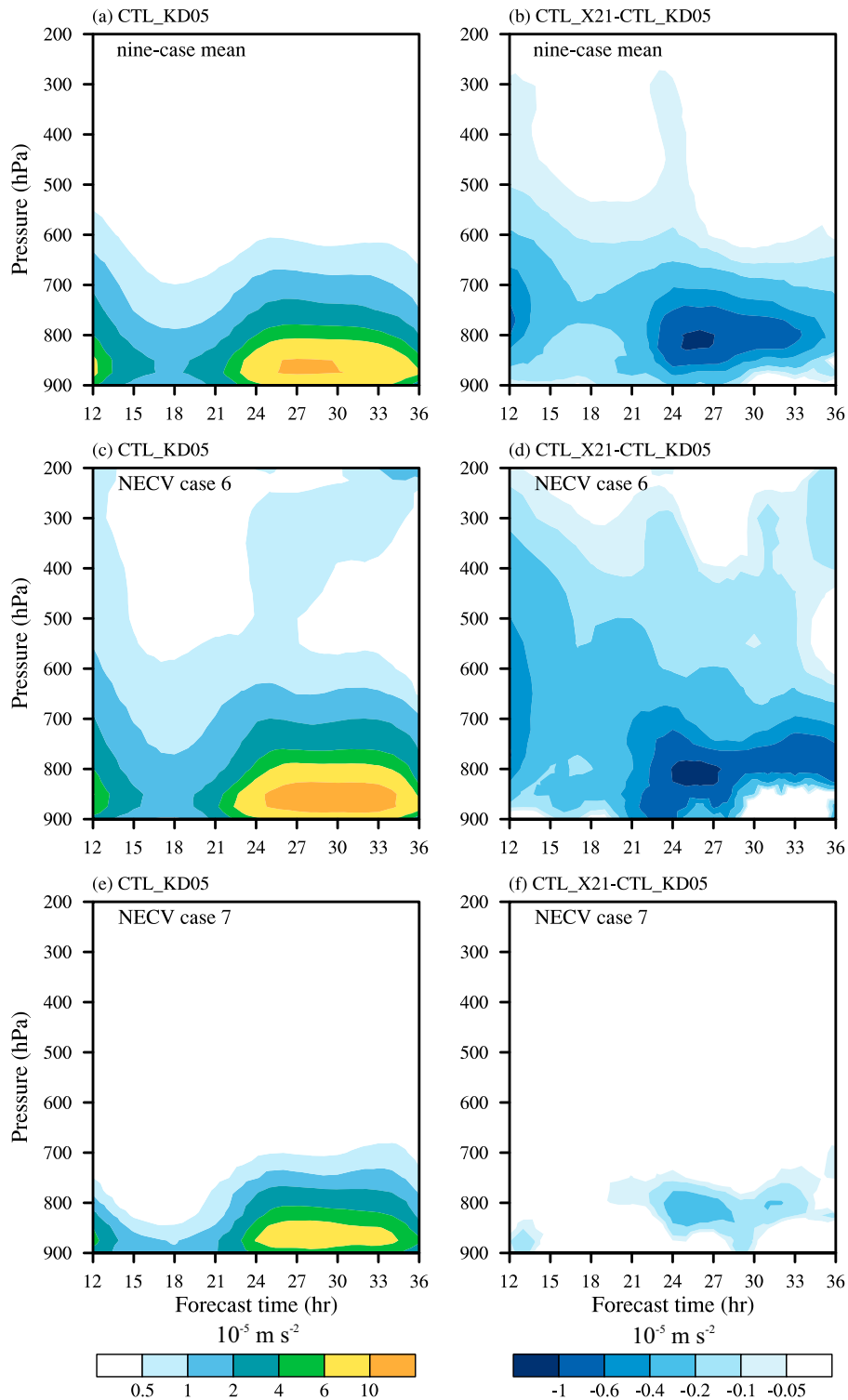
FIG. 9. Time–pressure plots of the nine-case mean (a) OGWD in CTL_KD05 averaged within the boxes encompassing the NECVs. (b) As in (a), but for the difference between CTL_X21 and CTL_KD05, i.e., CTL_X21 − CTL_KD05. The units are 10^{-5} m s^{-2}. (c),(d) and (e),(f) As in (a) and (b), but for the NECV cases 6 and 7, respectively.
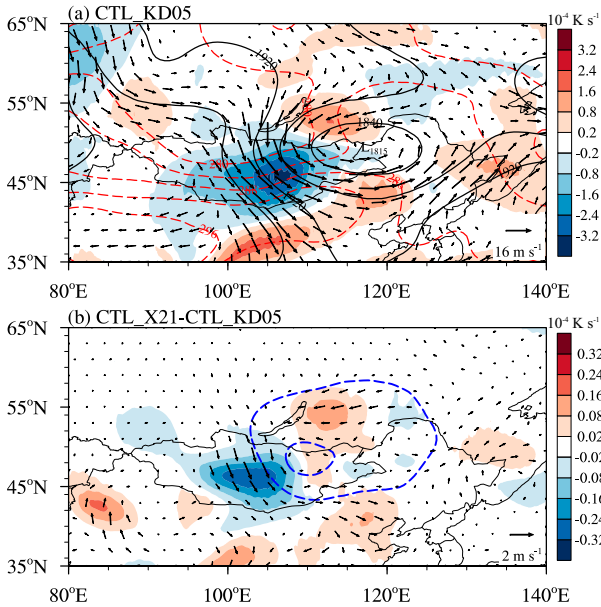
FIG. 10. (a) QG horizontal wind (vectors), GPH (black contours; gpm), temperature (red contours; K), and horizontal advection of temperature (shading; 10^{-4} K s^{-1}) at 800 hPa averaged between 24 and 30 h into the simulation on 5–7 Jul 2011 (i.e., NECV case 6) in the experiment CTL_KD05. (b) As in (a), but for the differences between the QG horizontal winds (vectors), GPHs (blue contours; gpm), and horizontal advection of temperature (shading; 10^{-4} K s^{-1}) in CTL_X21 and CTL_KD05, i.e., CTL_X21 − CTL_KD05.

increases, the distribution of horizontal Froude numbers above 0.1 becomes more and more extensive. For all these three resolutions, the centers of high Fr are located over the Mongolian Plateau to the south of Lake Baikal, but their magnitudes differ markedly. At 27-km resolution (Fig. 12a),

the largest Fr is less than 0.5, much smaller than that at 3-km resolution, which can exceed 1.5 (Fig. 12c). Moderate Fr between 0.5 and 1.0 is found in the 9-km resolution simulation (Fig. 12b). Theoretically, the NHE at 27-km resolution (Fig. 12d) reduce the OGWD by less than −5%, while much larger OGWD reductions by NHE of more than −70% are found at 3-km resolution (Fig. 12f). At 9-km resolution, there are moderate OGWD reductions by NHE of between −30% and −50% (Fig. 12e).

Figures 12g–i show the relative variations (in %) of column-integrated OGWD using the revised OGWD scheme compared to those using the original one. For reference, the column-integrated OGWD produced by the KD05 scheme is given in Figs. 12j–l. Overall, the spatial patterns and magnitudes of the relative variations of column-integrated OGWD are similar to their theoretical counterparts in Figs. 12d–f. Taking the 3-km resolution experiment as an example (Fig. 12i), the maximum relative variation occurs to the south of Lake Baikal, which exceeds −70%, in good agreement with that shown in Fig. 12f. While the NHE are expected to reduce the OGWD according to linear theory, positive variations of column-integrated OGWD are still found in a few isolated regions, similar to what could be seen in Fig. 7b. Nevertheless, the relative variations are predominantly negative and, more importantly, increase in magnitude (i.e., become more negative) as the model resolution increases (i.e., for finer grid spacings). The latter behavior is consistent with the theoretical results presented in Figs. 12d–f, suggesting that the NHE play a more vital role for the OGWD parameterization in high-resolution simulations. It is interesting to note that, for a unique set of adjustable parameters, the KD05 scheme tends to produce stronger OGWD as the resolution increases (Figs. 12j–l). This, which is consistent with the model behavior presented in Fig. 11 and discussed above, is
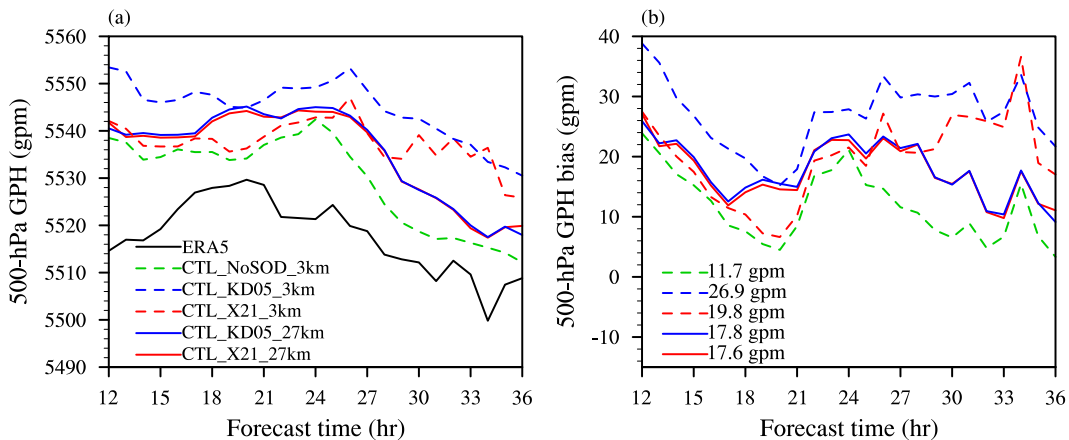

FIG. 11. Temporal evolution of (a) mean 500-hPa GPH (gpm) averaged within a box of 1° × 1° around the NECV center obtained from ERA5 reanalysis (black line) and the WRF simulations for 5–7 Jul 2011 (i.e., NECV case 6) using the original (blue lines) and revised (red lines) KD05 OGWD schemes at different resolutions (solid lines for 27-km and dashed lines for 3-km resolution). The green dashed line is for the 3-km resolution simulation without OGWD parameterization. (b) As in (a), but for the WRF Model biases with respect to ERA5. The numbers on the bottom-left corner of (b) indicate that the 500-hPa GPH biases averaged over the period of 12–36 h into the simulations.
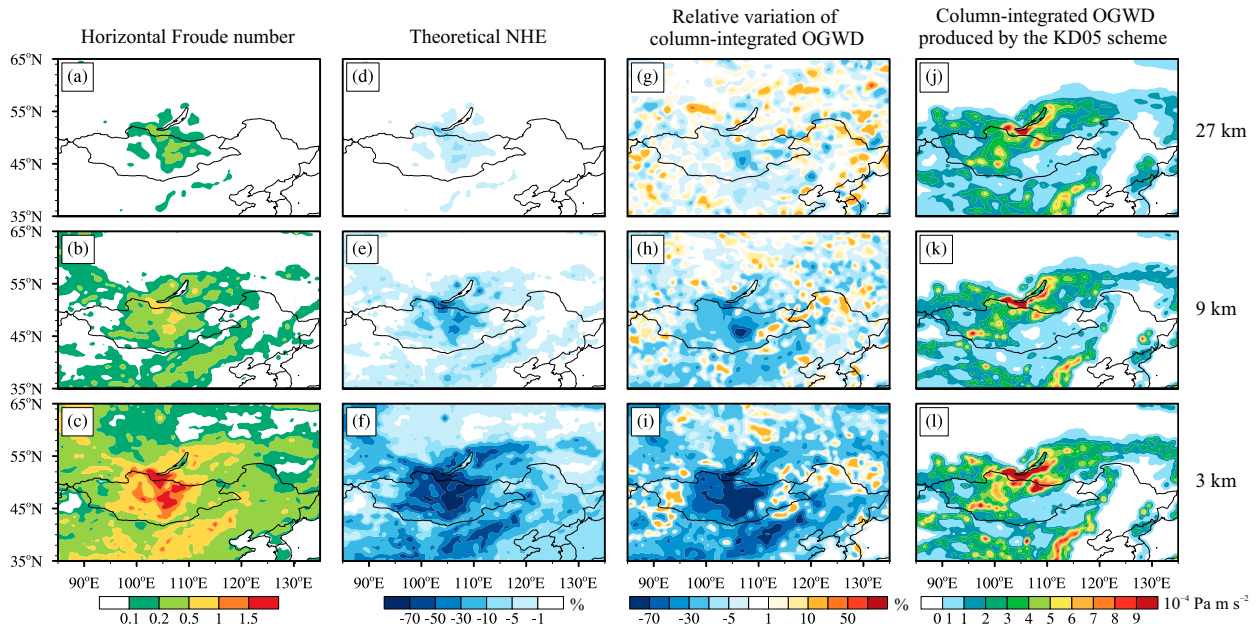
FIG. 12. Geographical distributions of (a)–(c) horizontal Froude number, (d)–(f) theoretical NHE correction (%), and (g)–(i) relative variation of column-integrated OGWD (%), i.e., (CTL_X21 − CTL_KD05)/CTL_KD05 × 100, averaged between 12 and 36 h into the simulations on 5–7 Jul 2011. (j)–(l) For reference, the column-integrated OGWD (10^{-4} Pa m s^{-2}) produced by the KD05 scheme is given. The first, second, and third rows are the simulations using resolutions of 27, 9, and 3 km, respectively.

because the reference-level stress is inversely proportional to the effective grid length λ_{eff} [see Eq. (1)], which needs to be carefully tuned in operational use (KD05). An alternative way to represent the SSO is by using Fourier transforms as suggested by van Niekerk and Vosper (2021) which is, however, not the focus of this work.

5. Summary and discussion

In this study, the KD05 orographic gravity wave drag (OGWD) parameterization scheme adopted in the WRF Model is revised by accounting for nonhydrostatic effects (NHE) on the surface wave momentum flux of upward-propagating OGWs according to the theoretical formulae derived in X21. Nine NECVs that occurred in the warm season (April–September) of 2011 in Northeast Asia are simulated using the WRF Model to evaluate the performance of the revised OGWD scheme in short-range weather forecast.

Results show that the WRF Model underestimates the intensities of the NECVs, with too high geopotential height (GPH). The model GPH biases are alleviated when using the revised OGWD scheme. For the nine-case average, the 500-hPa GPH bias is reduced by 9.7%, most of which comes from three NECVs that occurred in regions of complex terrain. The reduction of the 500-hPa GPH bias is up to 27% for these three cases. The role of the revised OGWD scheme in alleviating the GPH bias is confirmed by additional sensitivity experiments configured with different model physics (e.g., boundary layer and microphysics). Mechanisms were studied for the reduction of the model biases. In the revised OGWD scheme, the NHE can decrease the surface wave momentum flux of OGWs,

which tends to inhibit wave breaking and thus OGWD in the lower troposphere. The weakened OGWD directly strengthens the low-level horizontal winds, resulting in an enhancement of low-level cyclonic circulation of NCEVs and decreased GPH that alleviates the positive GPH bias in the lower troposphere. Concurrently, the posttrough cold advection strengthens, acting to deepen the NECV in the mid- and upper troposphere by thermal wind balance and hence reduce the positive GPH biases there. Furthermore, the NHE are found to be very sensitive to the model grid spacing. As the model's horizontal resolution increases, the parameterized OGWD is more and more weakened by the NHE.

These findings suggest that considering NHE in the OGWD parameterization scheme is beneficial for the simulation and short-range forecast of NECVs that occur in the complex-terrain region of Northeast Asia, in particular for numerical models of high-resolution (and thus with an OGWD parameterization dominated by narrow SSO). It should be noticed that the revised OGWD scheme has only been tested for a limited number of NECVs in the warm season. NECVs in the cold season when the OGWD is expected to be stronger, as well as other weather systems that occur in different mountainous regions (e.g., the Tibetan Plateau vortex), will be considered in the future.

Furthermore, the revised OGWD scheme considered herein only accounts for NHE in decreasing the surface wave momentum flux of upward-propagating OGWs. But the laterally dispersed wave energy can propagate to the upper atmosphere by a leakage effect and be absorbed downstream (Smith 1979; Durran et al. 2015) or propagate downstream within the boundary layer (Smith et al. 2006; Lott 2016; Xue and Giorgetta 2021). These effects have not been considered here. Given the

single-column approach commonly used in OGWD schemes, parameterizing these downstream effects is very challenging and deserves more study (Eichinger et al. 2023).

REFERENCES

Alexander, M. J., and Coauthors, 2010: Recent developments in gravity-wave effects in climate models and the global distribution of gravity-wave momentum flux from observations and models. *Quart. J. Roy. Meteor. Soc.*, **136**, 1103–1124, https://doi.org/10.1002/qj.637.

Alpert, J.-C., S.-Y. Hong, and Y.-J. Kim, 1996: Sensitivity of cyclogenesis to lower troposphere enhancement of gravity wave drag using the environmental modeling center medium range model. *Proc. 11th Conf. on Numerical Weather Prediction*, Norfolk, VA, Amer. Meteor. Soc., 322–323.

Barnes, S. L., 1973: Mesoscale objective map analysis using weighted time-series observations. NOAA Tech. Memo. ERL NSSL-62, 66 pp., https://repository.library.noaa.gov/view/noaa/17647/noaa_17647_DS1.pdf.

Beljaars, A. C. M., 1995: The parametrization of surface fluxes in large-scale models under free convection. *Quart. J. Roy. Meteor. Soc.*, **121**, 255–270, https://doi.org/10.1002/qj.49712152203.

Butchart, N., 2014: The Brewer-Dobson circulation. *Rev. Geophys.*, **52**, 157–184, https://doi.org/10.1002/2013RG000448.

Choi, H.-J., S.-J. Choi, M.-S. Koo, J.-E. Kim, Y. C. Kwon, and S.-Y. Hong, 2017: Effects of parameterized orographic drag on weather forecasting and simulated climatology over East Asia during boreal summer. *J. Geophys. Res. Atmos.*, **122**, 10 669–10 678, https://doi.org/10.1002/2017JD026696.

Collins, W., and Coauthors, 2004: Description of the NCAR Community Atmosphere Model (CAM 3.0). NCAR Tech. Note NCAR/TN-464+STR, 214 pp., https://doi.org/10.5065/D63N21CH.

Dee, D. P., and Coauthors, 2011: The ERA-Interim reanalysis: Configuration and performance of the data assimilation system. *Quart. J. Roy. Meteor. Soc.*, **137**, 553–597, https://doi.org/10.1002/qj.828.

Dudhia, J., 1989: Numerical study of convection observed during the winter monsoon experiment using a mesoscale two-dimensional model. *J. Atmos. Sci.*, **46**, 3077–3107, https://doi.org/10.1175/1520-0469(1989)046<3077:NSOCOD>2.0.CO;2.

Durran, D. R., M. O. G. Hills, and P. N. Blossey, 2015: The dissipation of trapped lee waves. Part I: Leakage of inviscid waves into the stratosphere. *J. Atmos. Sci.*, **72**, 1569–1584, https://doi.org/10.1175/JAS-D-14-0238.1.

Eichinger, R., and Coauthors, 2023: Emulating lateral gravity wave propagation in a global chemistry–climate model (EMAC v2.55.2) through horizontal flux redistribution. *Geosci. Model Dev.*, **16**, 5561–5583, https://doi.org/10.5194/gmd-16-5561-2023.

Fan, Z., M. Xue, K. Zhu, L. Luo, Z. Gao, and S. Li, 2023: Effects of precipitation latent heating on structure and evolution of northeast China cold vortex: A PV perspective. *J. Geophys. Res. Atmos.*, **128**, e2023JD039016, https://doi.org/10.1029/2023JD039016.

Fritts, D. C., and M. J. Alexander, 2003: Gravity wave dynamics and effects in the middle atmosphere. *Rev. Geophys.*, **41**, 1003, https://doi.org/10.1029/2001RG000106.

Grell, G. A., and S. R. Freitas, 2014: A scale and aerosol aware stochastic convective parameterization for weather and air quality modeling. *Atmos. Chem. Phys.*, **14**, 5233–5250, https://doi.org/10.5194/acp-14-5233-2014.

Hersbach, H., and Coauthors, 2018: ERA5 hourly data on pressure levels from 1959 to present. Copernicus Climate Change Service (C3S) Climate Data Store (CDS), accessed April to September 2011, https://doi.org/10.24381/cds.bd0915c6.

Hong, S.-Y., Y. Noh, and J. Dudhia, 2006: A new vertical diffusion package with an explicit treatment of entrainment processes. *Mon. Wea. Rev.*, **134**, 2318–2341, https://doi.org/10.1175/MWR3199.1.

Hu, K., R. Lu, and D. Wang, 2010: Seasonal climatology of cut-off lows and associated precipitation patterns over Northeast China. *Meteor. Atmos. Phys.*, **106**, 37–48, https://doi.org/10.1007/s00703-009-0049-0.

Iacono, M. J., J. S. Delamere, E. J. Mlawer, M. W. Shephard, S. A. Clough, and W. D. Collins, 2008: Radiative forcing by long-lived greenhouse gases: Calculations with the AER radiative transfer models. *J. Geophys. Res.*, **113**, D13103, https://doi.org/10.1029/2008JD009944.

Janjić, Z. I., 1994: The step-mountain Eta coordinate model: Further developments of the convection, viscous sublayer, and turbulence closure schemes. *Mon. Wea. Rev.*, **122**, 927–945, https://doi.org/10.1175/1520-0493(1994)122<0927:TSMECM>2.0.CO;2.

Jiménez, P. A., J. Dudhia, J. F. González-Rouco, J. Navarro, J. P. Montávez, and E. García-Bustamante, 2012: A revised scheme for the WRF surface layer formulation. *Mon. Wea. Rev.*, **140**, 898–918, https://doi.org/10.1175/MWR-D-11-00056.1.

Kim, Y.-J., and A. Arakawa, 1995: Improvement of orographic gravity wave parameterization using a mesoscale gravity wave model. *J. Atmos. Sci.*, **52**, 1875–1902, https://doi.org/10.1175/1520-0469(1995)052<1875:IOOGWP>2.0.CO;2.

——, and J. D. Doyle, 2005: Extension of an orographic-drag parametrization scheme to incorporate orographic anisotropy and flow blocking. *Quart. J. Roy. Meteor. Soc.*, **131**, 1893–1921, https://doi.org/10.1256/qj.04.160.

——, S. D. Eckermann, and H. Y. Chun, 2003: An overview of the past, present and future of gravity-wave drag parametrization

for numerical climate and weather prediction models. *Atmos.–Ocean*, **41**, 65–98, https://doi.org/10.3137/ao.410105.

Klemp, J. B., and D. R. Durran, 1983: An upper boundary condition permitting internal gravity wave radiation in numerical mesoscale models. *Mon. Wea. Rev.*, **111**, 430–444, https://doi.org/10.1175/1520-0493(1983)111<0430:AUBCPI>2.0.CO;2.

Kruse, C. G., and Coauthors, 2022: Observed and modeled mountain waves from the surface to the mesosphere near the Drake Passage. *J. Atmos. Sci.*, **79**, 909–932, https://doi.org/10.1175/JAS-D-21-0252.1.

Lian, Y., B. Shen, S. Li, G. Liu, and X. Yang, 2016: Mechanisms for the formation of Northeast China cold vortex and its activities and impacts: An overview. *J. Meteor. Res.*, **30**, 881–896, https://doi.org/10.1007/s13351-016-6003-4.

Lott, F., 2016: A new theory for downslope windstorms and trapped mountain waves. *J. Atmos. Sci.*, **73**, 3585–3597, https://doi.org/10.1175/JAS-D-15-0342.1.

——, and M. J. Miller, 1997: A new subgrid-scale orographic drag parametrization: Its formulation and testing. *Quart. J. Roy. Meteor. Soc.*, **123**, 101–127, https://doi.org/10.1002/qj.49712353704.

Lu, Y., T. Wu, X. Xu, L. Zhang, and M. Chu, 2020: Improved simulation of the Antarctic stratospheric final warming by modifying the orographic gravity wave parameterization in the Beijing climate center Atmospheric General Circulation Model. *Atmosphere*, **11**, 576, https://doi.org/10.3390/atmos11060576.

Luo, L., M. Xue, K. Zhu, and B. Zhou, 2018: Explicit prediction of hail in a long-lasting multicellular convective system in eastern China using multimoment microphysics schemes. *J. Atmos. Sci.*, **75**, 3115–3137, https://doi.org/10.1175/JAS-D-17-0302.1.

Matsui, S., and Coauthors, 2018: Neuronal SIRT1 regulates macronutrient-based diet selection through FGF21 and oxytocin signalling in mice. *Nat. Commun.*, **9**, 4604, https://doi.org/10.1038/s41467-018-07033-z.

McFarlane, N. A., 1987: The effect of orographically excited gravity wave drag on the general circulation of the lower stratosphere and troposphere. *J. Atmos. Sci.*, **44**, 1775–1800, https://doi.org/10.1175/1520-0469(1987)044<1775:TEOOEG>2.0.CO;2.

McLandress, C., T. G. Shepherd, S. Polavarapu, and S. R. Beagley, 2012: Is missing orographic gravity wave drag near 60°S the cause of the stratospheric zonal wind biases in chemistry-climate models? *J. Atmos. Sci.*, **69**, 802–818, https://doi.org/10.1175/JAS-D-11-0159.1.

Meng, Z., and Coauthors, 2018: The deadliest tornado (EF4) in the past 40 years in China. *Wea. Forecasting*, **33**, 693–713, https://doi.org/10.1175/WAF-D-17-0085.1.

Miranda, P. M. A., and I. N. James, 1992: Non-linear three-dimensional effects on gravity-wave drag: Splitting flow and breaking waves. *Quart. J. Roy. Meteor. Soc.*, **118**, 1057–1081, https://doi.org/10.1002/qj.49711850803.

Morrison, H., G. Thompson, and V. Tatarskii, 2009: Impact of cloud microphysics on the development of trailing stratiform precipitation in a simulated squall line: Comparison of one- and two-moment schemes. *Mon. Wea. Rev.*, **137**, 991–1007, https://doi.org/10.1175/2008MWR2556.1.

Nakanishi, M., and H. Niino, 2006: An improved Mellor–Yamada level-3 model: Its numerical stability and application to a regional prediction of advection fog. *Bound.-Layer Meteor.*, **119**, 397–407, https://doi.org/10.1007/s10546-005-9030-8.

Nieto, R., and Coauthors, 2005: Climatological features of cutoff low systems in the Northern Hemisphere. *J. Climate*, **18**, 3085–3103, https://doi.org/10.1175/JCLI3386.1.

Palmer, T. N., G. J. Shutts, and R. Swinbank, 1986: Alleviation of a systematic westerly bias in general circulation and numerical weather prediction models through an orographic gravity wave drag parametrization. *Quart. J. Roy. Meteor. Soc.*, **112**, 1001–1039, https://doi.org/10.1002/qj.49711247406.

Pleim, J. E., 2007: A combined local and nonlocal closure model for the atmospheric boundary layer. Part I: Model description and testing. *J. Appl. Meteor. Climatol.*, **46**, 1383–1395, https://doi.org/10.1175/JAM2539.1.

Polichtchouk, I., N. Wedi, and Y.-H. Kim, 2021: Resolved gravity waves in the tropical stratosphere: Impact of horizontal resolution and deep convection parametrization. *Quart. J. Roy. Meteor. Soc.*, **148**, 233–251, https://doi.org/10.1002/qj.4202.

Sandu, I., and Coauthors, 2019: Impacts of orography on large-scale atmospheric circulation. *npj Climate Atmos. Sci.*, **2**, 10, https://doi.org/10.1038/s41612-019-0065-9.

Scinocca, J. F., and N. A. McFarlane, 2000: The parametrization of drag induced by stratified flow over anisotropic orography. *Quart. J. Roy. Meteor. Soc.*, **126**, 2353–2393, https://doi.org/10.1002/qj.49712656802.

Skamarock, W. C., J. B. Klemp, M. G. Duda, L. D. Fowler, S.-H. Park, and T. D. Ringler, 2012: A multiscale nonhydrostatic atmospheric model using centroidal Voronoi Tesselations and C-Grid staggering. *Mon. Wea. Rev.*, **140**, 3090–3105, https://doi.org/10.1175/MWR-D-11-00215.1.

——, and Coauthors, 2019: A description of the advanced research WRF model version 4. NCAR Tech. Note NCAR/TN-556+STR, 162 pp., https://doi.org/10.5065/1dfh-6p97.

Smith, R., 1979: The influence of the Earth's rotation on mountain wave drag. *J. Atmos. Sci.*, **36**, 177–180, https://doi.org/10.1175/1520-0469(1979)036<0177:TIOTER>2.0.CO;2.

——, Q. Jiang, and J. D. Doyle, 2006: A theory of gravity wave absorption by a boundary layer. *J. Atmos. Sci.*, **63**, 774–781, https://doi.org/10.1175/JAS3631.1.

Sun, L., X. Y. Zheng, and Q. Wang, 1994: The climatological characteristics of northeast cold vortex in China (in Chinese). *J. Appl. Meteor. Sci.*, **5**, 297–303.

Tewari, M., and Coauthors, 2004: Implementation and verification of the unified Noah land surface model in the WRF model [presentstion]. *20th Conf. on Weather Analysis and Forecasting/16th Conf. on Numerical Weather Prediction*, Seattle, WA, Amer. Meteor. Soc., 14.2a, https://ams.confex.com/ams/84Annual/techprogram/paper_69061.htm.

Thompson, G., P. R. Field, R. M. Rasmussen, and W. D. Hall, 2008: Explicit forecasts of winter precipitation using an improved bulk microphysics scheme. Part II: implementation of a new snow parameterization. *Mon. Wea. Rev.*, **136**, 5095–5115, https://doi.org/10.1175/2008MWR2387.1.

van Niekerk, A., and S. Vosper, 2021: Towards a more "scale-aware" orographic gravity wave drag parametrization: Description and initial testing. *Quart. J. Roy. Meteor. Soc.*, **147**, 3243–3262, https://doi.org/10.1002/qj.4126.

Webster, S., A. R. Brown, D. R. Cameron, and C. P. Jones, 2003: Improvements to the representation of orography in the Met Office Unified Model. *Quart. J. Roy. Meteor. Soc.*, **129**, 1989–2010, https://doi.org/10.1256/qj.02.133.

Wei, P., and Coauthors, 2023: On the key dynamical processes supporting the 21.7 Zhengzhou record-breaking hourly rainfall in China. *Adv. Atmos. Sci.*, **40**, 337–349, https://doi.org/10.1007/s00376-022-2061-y.

Xu, X., R. Li, M. A. C. Teixeira, and Y. Lu, 2021: On the momentum flux of vertically propagating orographic gravity waves excited in nonhydrostatic flow over three-dimensional

orography. *J. Atmos. Sci.*, **78**, 1807–1822, https://doi.org/10. 1175/JAS-D-20-0370.1.

——, and Coauthors, 2023a: Reducing winter precipitation biases over the western Tibetan Plateau in the Model for Prediction Across Scales (MPAS) with a revised parameterization of orographic gravity wave drag. *J. Geophys. Res. Atmos.*, **128**, e2023JD039123, https://doi.org/10.1029/2023JD039123.

——, M. Li, S. Zhong, and Y. Wang, 2023b: Impact of parameterized topographic drag on a simulated northeast China cold vortex. *J. Geophys. Res. Atmos.*, **128**, e2022JD037664, https:// doi.org/10.1029/2022JD037664.

——, and Coauthors, 2024: A parametrization scheme accounting for nonhydrostatic effects on vertically propagating orographic gravity waves: Formulae and preliminary tests in the Model for Prediction Across Scales (MPAS). *J. Atmos. Sci.*, **81**, 805– 817, https://doi.org/10.1175/JAS-D-23-0020.1.

Xue, H., and M. A. Giorgetta, 2021: A large-eddy simulation study on the diurnally evolving nonlinear trapped lee waves over a two-dimensional steep mountain. *J. Atmos. Sci.*, **78**, 399–415, https://doi.org/10.1175/JAS-D-20-0085.1.

Yang, B., and L. Wang, 2021: Statistical characteristics and causes of different types of northeast cold vortex from May to September (in Chinese). *Daqi Kexue Xuebao*, **44**, 773–781.

Zängl, G., 2003: Orographic gravity waves close to the nonhydrostatic limit of vertical propagation. *J. Atmos. Sci.*, **60**, 2045–2063, https:// doi.org/10.1175/1520-0469(2003)060<2045:OGWCTT>2.0.CO;2.

——, D. Reinert, P. Rípodas, and M. Baldauf, 2015: The ICON (ICOsahedral Non-hydrostatic) modelling framework of DWD and MPI-M: Description of the non-hydrostatic dynamical core. *Quart. J. Roy. Meteor. Soc.*, **141**, 563–579, https://doi.org/ 10.1002/qj.2378.

Zhang, R., X. Xu, and Y. Wang, 2020: Impacts of subgrid orographic drag on the summer monsoon circulation and precipitation in East Asia. *J. Geophys. Res. Atmos.*, **125**, e2019JD032337, https:// doi.org/10.1029/2019JD032337.

Zhou, X., A. Beljaars, Y. Wang, B. Huang, C. Lin, Y. Chen, and H. Wu, 2017: Evaluation of WRF simulations with different selections of subgrid orographic drag over the Tibetan Plateau. *J. Geophys. Res. Atmos.*, **122**, 9759–9772, https://doi.org/ 10.1002/2017JD027212.